energy&fuels

Article

Cite This: Energy Fuels 2019, 33, 7385−7397

pubs.acs.org/EF

Detailed One-Dimensional Model for Steam-Biomass Gasification in a Bubbling Fluidized Bed

Cornelius E. Agu,*[,†] Christoph Pfeifer,[‡] Marianne Eikeland,[†] Lars-Andre Tokheim,[†] and Britt M.E. Moldestad[†]

[†]Department of Process, Energy and Environmental Technology, University of South-Eastern Norway, 3918 Porsgrunn, Norway

[‡]Department of Material Sciences and Process Engineering, University of Natural Resources and Life Sciences, 1190 Vienna, Austria

Supporting Information

ABSTRACT: A one-dimensional unsteady state model is developed for simulation of biomass gasification in a bubbling fluidized bed. The proposed model accounts for the effect of hydrodynamic behavior of the fluidized bed by incorporating the momentum equations of fluid and fuel particles. The model results are validated against experimental data in the literature as well as the results from existing models. The proposed model is capable of predicting the total gas yield and composition of the product gas at different operating conditions. The effect of biomass feeding position is investigated, and the performance of a reactor under nonisothermal conditions is compared with its performance under isothermal operation. As the developed model is computationally less demanding, it can be used to improve design and operational control of bubbling fluidized bed gasifiers.

1. INTRODUCTION

Modeling and simulation of biomass gasification reactors is still a growing area of research. For a continuous process and a steady product quality, biomass gasification can be carried out in a bubbling fluidized bed[1] or a circulating fluidized bed reactor.[2,3] An entrained flow reactor can also be applied using a pulverized feedstock.[4] Moreover, the so-called dual fluidized bed systems are available, which combine two circulating beds or one bubbling and one circulating bed. Depending on the desired product gas composition, biomass gasification can be achieved using air (or pure oxygen), steam, or carbon dioxide as the gasifying agent. For higher energy efficiency, it is advantageous to apply a combination of steam and air.[5] Gonzalez-Vazquez et al.[5] showed that an optimum syngas yield of 2.0 m^3/kg biomass containing 35% (H_2 + CO) can be obtained in an atmospheric wood gasifier when the steam to air ratio of 3.0 is used.

Due to experimental setup limitations, different models have been developed to investigate the effect of different process parameters and operating conditions on the syngas production rate, composition, and energy value. Modeling of a fluidized bed biomass gasifier is a complex task due to the different phase interactions (solid−gas and solid−solid interactions) in the bed. Mazaheri et al.[6] suggested a procedure for achieving a successful model for biomass gasification at different operating conditions. A gasification model can be based on a thermodynamic equilibrium assumption or on chemical reaction kinetics. While the former does not provide information about the reactor design and can only be applied for a specific reaction route, a model based on the chemical kinetics accounts for the reactor geometry and is also flexible to accommodate as many different reactions as possible. A thermodynamic equilibrium model is usually based on minimization of Gibbs free energy, and it gives the maximum theoretical gas yields under a given operating condition.[7] The most complex and reliable kinetic models are those based on the conservation of mass, momentum, and energy of fluid and particles. A combination of thermodynamic equilibrium and kinetic models has also been demonstrated in different studies.[8] Pauls et al.[8] incorporated the reaction kinetics and the bed hydrodynamics to enhance CO and H_2 production.

Different multidimensional numerical approaches including the two-fluid model (TFM),[9] computational fluid dynamics coupled with discrete element method (CFD-DEM),[10] and multiphase particle-in-cell (MP-PIC)[11] can be used to model the biomass reactor. In the TFM, both the gas and solid phases are processed as continuous phases, making it faster than the other two approaches. The CFD-DEM requires extensive computational resources due to the extremely small time step required to resolve the particle collisions. In the MP-PIC approach, the solid motion is described in the Lagrangian frame where a computational particle represents a large number of particles, which have similar properties. The grouping of particles in the MP-PIC system makes the simulation faster, thereby increasing its application to industrial scale. Depending on the solution method, results from different studies using the 3D[1,4,12] and 2D[13,14] versions of the models agree very well with experiments. However, the complexities arising from the multidimensional models limit their applications. The models are computationally time demanding, requiring several days to obtain a solution in some seconds of simulation time.

To reduce the gasification modeling challenges, different versions of 1D (steady and unsteady state) models have been proposed.[15,16] Most of these models are based on the two-phase theory.[17] The two-phase theory models solve only the mass and energy balances in two separate phases (bubble and emulsion) coupled with the exchange of the conserved variables at the interface between the two phases. The hydrodynamics of the bed are captured by the use of bubble velocity, bubble volume

Received: April 28, 2019
Revised: July 6, 2019
Published: July 8, 2019

DOI: 10.1021/acs.energyfuels.9b01340
Energy Fuels 2019, 33, 7385−7397

fraction, and bed voidage in the interface transfer models. In some studies,[16] attempts are made to incorporate the fluid velocity model due to change of mass of each species in the bed. Hejazi et al.[16] also included an expression for solid circulation rate in the model developed for a dual fluidized bed biomass gasifier. To minimize the potential effect of reverse reactions, Inayat et al.[18] implemented a CO_2 adsorbent in their kinetic model, which enhances the production of hydrogen. As most of the available models are based on the assumption of a uniform distribution of the fuel particles, the two-phase models fail to properly account for the axial distribution of temperature and materials in the reactor. Moreover, extensive one-dimensional models based on conservation of mass, momentum, and energy have also been developed for simulation of fluidized bed reactors.[19,20] These 1D models include the equations for the inert particle momentum and solid fraction propagation, making it more computational demanding than the two-phase theory model. For a typical entrained flow condition, Miccio[21] presented a steady state 1D model that accounts for char fragmentation during the gasification process.

To further enhance the modeling and simulation of biomass gasifiers for efficient design and operation, a more simplified but realistic one-dimensional unsteady state model is developed in the present study. The proposed model includes the momentum equations of the fluid and fuel particles to capture the effect of particle properties on the bed behavior. In the model development, it is assumed that the bed inert particles have zero mean velocity over the bed height. This assumption helps to eliminate the complexities in decoupling the inert particle motion from the rest of the bed. To account for the effects of rising bubbles, correlations for predicting the bed expansion, bubble velocity, and bubble volumetric flux are incorporated. The fluid is modeled based on the Eulerian approach while the fuel particle motion is based on the single particle motion. The effects of the kinetic energy change, and the impact of bubble flow and resistance due to collision with the bed inert particles are considered in the solid fuel motion. The approach introduced in this paper for modeling biomass gasification process helps to improve the widely applied existing simplified models. The two-phase theory model usually assumes isothermal conditions in which the solid and gas phases have the same temporal temperature, neglecting the possible heat resistance accompanied by energy exchange between two different materials. Based on the uniform distribution of solids, the effect of fuel particle properties such as size and density are not considered in the models based on the two-phase theory. It should be noted that particle segregation in bubbling fluidized bed is mainly influenced by the particle size and bulk density.[22] Thus, neglecting the particle properties may result in the effect of fluidized bed hydrodynamics not being properly accounted for during the gasification process. Obviously, segregation behavior is very difficult to model due to the complex mechanisms surrounding the phenomenon.[23] However, tracking the motion of the solid fuel subject to interactions with inert particles and gas species can help to achieve distribution of the fuel particles to some extent. Hence, the proposed model can be used to investigate the behavior of a gasifier at different operating conditions and design choices. In the subsequent sections, the detailed development of the model is presented and the model results are validated against experimental data from the literature and results from some existing models.

2. MODEL DESCRIPTION

The model proposed in this study for computation of biomass gasification process is based on the chemical kinetics. Since gasification proceeds after biomass pyrolysis, which can be completed over a significant length of time, both stages of biomass conversion in a bubbling bed are taken into account.

2.1. Gasification and Reaction Kinetics. Biomass gasification depends on temperature and time and proceeds after pyrolysis where the fuel particles are thermally broken down into volatiles, tar, and char. For a lignin-based biomass, the pyrolysis takes place within 250−500 °C.[24] The biomass conversion in a fluidized bed increases the total gas flow rate and the solids inventory in the bed, which can be obtained at a given temperature by considering the reaction kinetics. There are several kinetic models for biomass pyrolysis, but the scheme demonstrated in Figure 1 can be applied.[25]

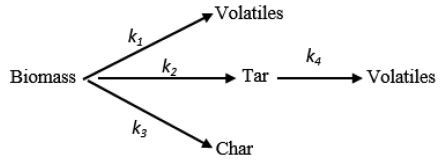

Figure 1. Illustration of the three parallel steps in biomass pyrolysis.

The kinetic rate constant k for the different stages in the pyrolysis phase can be expressed in the Arrhenius form.

$$k_i = A_i \exp\left(-\frac{E_i}{RT}\right) \tag{1}$$

Here, i = 1, 2, 3, 4 is the index indicating each of the reactions involved in the pyrolysis process. Values of the frequency factor A and the activation energy E can be obtained from the work of Chan et al.[26] as reported in Table 1. The biomass pyrolysis can also be assumed to be endothermic with a reaction enthalpy of 64 kJ/kg.[16]

Table 1. Parameters for Kinetic Rate Constant in the Biomass Pyrolysis[16,26]

pyrolysis step, i	A_i (1/s)	E_i (kJ/mol)
1	1.30×10^8	140
2	2.00×10^8	133
3	1.08×10^7	121
4	1.00×10^5	93.3

The mole fraction ϑ_j of the volatiles $j \in (H_2, CO, CO_2, CH_4)$ in the primary pyrolysis $(i = 1)$ can be obtained from eq 2.[14]

$$\vartheta_j = \frac{\Lambda_j}{\sum_j \Lambda_j}; \quad \Lambda_j = c_j T^{a_j} \tag{2}$$

Here, T is the mean temperature of the bed, and c_j and a_j are model fitting parameters for each gas species as outlined in Table 2. The correlation in eq 2 for the uncorrected gas mole fraction Λ_j was obtained in the temperature range 1000−1070 K based on the experimental data from pine wood pellets.[14] The mass fraction γ_j of each component $j \in (H_2, CO, CO_2, CH_4, \text{inert})$ resulting from the tar cracking $(i = 4)$ is also given in Table 2.[16]

Beyond the pyrolysis, the resulting char particles react with the available gasifying agent including oxygen, steam, and carbon dioxide. Moreover, the permanent gas components in the

DOI: 10.1021/acs.energyfuels.9b01340
Energy Fuels 2019, 33, 7385−7397

Table 2. Parameters for the Light Gases from Biomass Pyrolysis[14,16]

gas species, j	c_j	a_j	γ_j
H_2	1.34×10^{-16}	5.73	0.02
CO	1.80×10^{7}	−1.87	0.56
CO_2	2.48×10^{3}	−0.70	0.11
CH_4	4.43×10^{5}	−1.50	0.09
inert			0.22

volatiles also act as gasifying agents. A number of gas phase (homogeneous) reactions also take place in the reactor. Different kinetic rate constant models are available for each of the reactions depending on the available gasifying agents. For a steam biomass gasification, Table 3 describes some of the most favorable reactions with their kinetic rate constants taken from different publications.

2.2. Computational Model Development. The distribution of temperature and materials in a bubbling fluidized bed reactor depends on the hydrodynamic behavior of the bed. To account for this behavior, both the solid and gas momentum equations are considered in addition to the mass balance of each phase in the flow direction. Modeling of gas flow is based on the Eulerian approach while the fuel particle motion is based on the dispersed flow behavior. Due to changes in the mass of the fuel particles, the kinetic energy change along the flow direction is incorporated in the fuel particle flow model. The particle−particle collisions and dragging of particles by the bubbles are also accounted for. Figure 2 describes the flows of gas and fuel particles within the bed and across their respective boundaries. The term u_B is the bubble rise velocity, and u and v are the gas and solid fuel velocities, respectively. $\dot{m}_{g,\mathrm{in}}$ and $\dot{m}_{b,\mathrm{in}}$ are the respective gas and biomass mass flow rates at the inlets with $T_{g,\mathrm{in}}$ and $T_{b,\mathrm{in}}$ as the corresponding boundary temperatures. D is the reactor diameter, l_{sb} is the biomass feeding height above the distributor, and L and l_f are the total reactor height and bed height at the fluidized state, respectively.

In addition to the assumptions outlined below, the necessary simplifications introduced in developing the gasifier model are given in the relevant sections.

- There are no variations of temperature and species in the radial directions. Hence, the model is one-dimensional, i.e. there are only gradients in the axial direction.
- The bed expands uniformly, resulting in an even distribution of average bed particles. With this assumption, the complex computation of mass flow of inert particles can be eliminated while the average solids fraction of the bed can be obtained from the available empirical correlations.
- The bed inert material remains inert over a clearly defined volume, and there is no mass loss due to entrainment. It should be noted that in the absence of entrainment, inert particles can experience a wide range of velocities (in axial direction) ranging from a negative value corresponding to their downward movement in the annulus to about bubble rise velocity for those of them that are carried upward with bubbles. For simplicity, the net velocity of the inert particles is considered zero over one cycle of the solids circulation.

Table 3. Kinetic Rate Constants for Different Reactions in Steam-Biomass Gasification[a]

i	reactions	ΔH_{ri}^0 (kJ/mol)	rate constant, r_i (mol/m^3·s)	ref(s)
		Heterogeneous		
5	$C + H_2O \rightarrow CO + H_2$	+131	$r_5 = \frac{k_{r5,1}x_{H_2O}}{1/p + k_{r5,2}x_{H_2} + k_{r5,3}x_{H_2O}}(1 - X_c)[C]$	27
			$k_{r5,1} = 1.25 \times 10^5 \exp\left(-\frac{28000}{T}\right)$	
			$k_{r5,2} = 3.26 \times 10^{-4}$	
			$k_{r5,3} = 0.313 \exp\left(-\frac{10120}{T}\right)$	
6	$C + CO_2 \rightarrow 2CO$	+172	$r_6 = \frac{k_{r6,1}}{1 + \frac{x_{CO}}{k_{r6,2}x_{CO_2}}}[C]$	28
			$k_{r6,1} = 3.6 \times 10^5 \exp\left(-\frac{20130}{T}\right)$	
			$k_{r6,2} = 4.15 \times 10^3 \exp\left(-\frac{11420}{T}\right)$	
7	$C + 2H_2 \rightarrow CH_4$	−75	$r_7 = 6.11 \times 10^{-3} \exp\left(-\frac{80333}{RT}\right)[H_2][C]$	29
		Homogeneous		
8	$CO + H_2O \leftrightarrow CO_2 + H_2$	−41	$r_8 = 0.278 \exp\left(-\frac{12560}{RT}\right)\left\{[H_2O][CO] - \frac{[H_2O][CO]}{k_{eq,8}}\right\}$	30
			$k_{eq,8} = 0.022 \exp\left(\frac{34730}{RT}\right)$	
9	$CH_4 + H_2O \rightarrow CO + 3H_2$	+206	$r_9 = 312 \exp\left(-\frac{15098}{T}\right)[CH_4]$	31

[a] [ ] = molar concentration (mol/m^3), p (Pa) = pressure, and X_c = char conversion factor.

DOI: 10.1021/acs.energyfuels.9b01340
Energy Fuels 2019, 33, 7385−7397

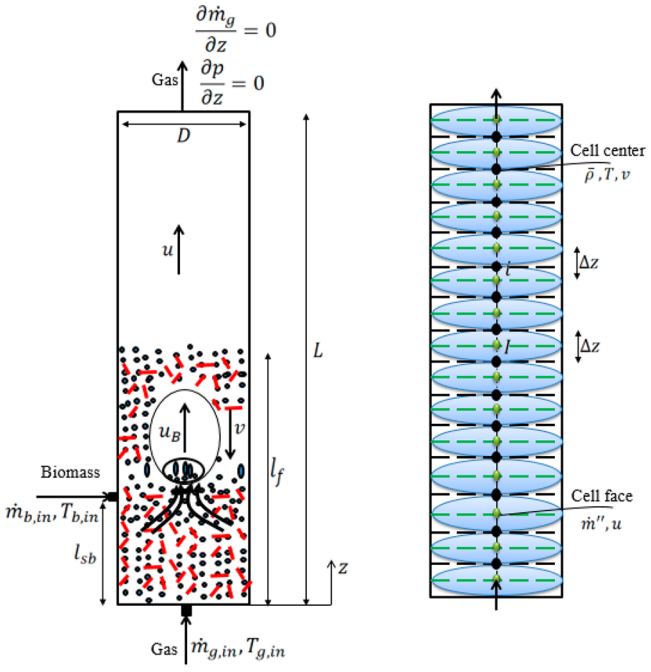

Figure 2. (a) Illustration of bubbling fluidized bed behavior in a binary solid mixture (red = fuel particles (s), black = bed inert material (p)), showing biomass and gas boundary conditions and drag of solids into the bubble wake. (b) Division of the reactor into different units of computational volume of height Δz, showing the cell center (i) and cell face (I) for storage of different flow variables.

- The ash content of biomass is negligible.
- The unconverted tar is in vapor phase.
- The gas species move upward while the fuel solids move downward.

2.2.1. Species Mass Balance. Considering a continuum flow of solid fuel particles, the rate of change in the concentration of the particles within a given volume can be described by

$$\frac{\partial \bar{\rho}_{s,j}}{\partial t} = -\frac{\partial (v\bar{\rho}_{s,j})}{\partial z} + S_{s,j} \tag{3}$$

where $\bar{\rho}_{s,j}$ is the mass concentration of fuel particles $j \in$ (b, c), with "b" and "c" denoting biomass and char, respectively, and $S_{s,j}$ is the rate of generation of mass of the species.

Similarly, the mass balance for each of the gas species $j \in$ (H_2, CO, CO_2, CH_4, H_2O, tar) is as described below.

$$\frac{\partial \bar{\rho}_{g,j}}{\partial t} = -\frac{\partial (y_j \dot{m}_g'')}{\partial z} + S_{g,j} \tag{4}$$

$$y_j = \frac{\bar{\rho}_{g,j}}{\bar{\rho}_g} \tag{5}$$

Here, $S_{g,j}$ is the rate of generation of the gas species per unit volume and $\dot{m}_g'' = u\bar{\rho}_g$ is the mass flux of the bulk gas. The mass concentration of the gas mixture $\bar{\rho}_g$ is given by

$$\frac{\partial \bar{\rho}_g}{\partial t} = -\frac{\partial (\dot{m}_g'')}{\partial z} + \sum S_{g,j} \tag{6}$$

2.2.2. Momentum Balance. The velocities of the solid fuel particles and gas species can be obtained by balancing the forces across the control volume for each phase. The Lagrangian approach is considered for the solid fuel where the motion of each particle is assumed to be independent of the others. The gas flow follows the continuum mechanism, and thus the Eulerian approach is used for this phase. In principle, the conservative model developed in the Eulerian frame can be converted to a nonconservative Lagrangian model by differentiating appropriately the partial differential (flux) terms. For the solid momentum equation, the resulting model is similar to the Newton's second law of motion that links the external forces acting on the particle to the resultant force causing the particle acceleration.

2.2.2.1. Solid Phase. With the assumption that the solid fuel particles are dispersed within the bed, the single particle downward motion is described as follows:

$$\rho_s \frac{\partial v}{\partial t} = -\rho_s v \frac{\partial v}{\partial z} + g(\rho_s - \rho_g) + F_B' + \beta_{g,s}(-u - v) + \beta_{p,s}(-v) + v\sum S_{s,j} \tag{7}$$

where ρ_s and ρ_g are the solid and gas densities, respectively, g is the acceleration due to gravity, and F_B' is the force per unit volume exerted on the fuel particles by the inert bed material due to flow of bubbles. $\beta_{g,s}$ and $\beta_{p,s}$ are the momentum transfer coefficients due to drag by the gas and collision with the inert particles, respectively. Equation 7 is developed based on Newton's second law of motion, where the term on the left accounts for the acceleration of the fuel particles and the first term on the right is the momentum change accompanied by a change in the particle kinetic energy. Other terms on the right side account for the total external forces acting on the particles. Starting from the second term on the right, the external forces include the buoyancy force, momentum exchange with the fluidized inert particles dragged into the bubble wake, momentum exchange with fluid flowing in the opposite direction, and momentum exchange due to collision with static inert particles. The last term is the momentum generated due to changes in the mass of the fuel particle during conversion. Moreover, different other terms including the virtual mass acceleration and fluid pressure forces can also be included in eq 7, but because of their relatively small contributions, these terms are not considered in this paper.

$$\beta_{g,s} = \frac{6D_R}{\pi d_s^3} \tag{8}$$

The drag resistance D_R with the gas−solid drag coefficient C_d and particle Reynold number Re_s can be obtained from the following expressions.[32]

$$D_R = \frac{1}{8}\pi d_s^2 \rho_g C_d |u + v| \tag{9}$$

$$C_d = \frac{24}{Re_s}[1 + (8.1716\exp(-4.0655\varphi_s))Re_s^{0.0964+0.5565\varphi_s}] + \frac{73.69Re_s\exp(-5.0748\varphi_s)}{Re_s + 5.378\exp(6.2122\varphi_s)} \tag{10}$$

$$Re_s = \frac{\rho_g d_s}{\mu_g}|u + v| \tag{11}$$

DOI: 10.1021/acs.energyfuels.9b01340
Energy Fuels 2019, 33, 7385−7397

where φ_s is the mean sphericity of the fuel particles. The average diameter d_s and density ρ_s of the solid fuel are given by

$$d_s = \frac{d_b}{[1 + (1.25\sqrt[3]{n_1\Psi(1 - X_c)} - 1)y_{s,c}]} \tag{12}$$

$$\rho_s = \left(\frac{y_{sc}}{\rho_c} + \frac{(1 - y_{sc})}{\rho_b}\right)^{-1} \tag{13}$$

Equation 12 is derived considering the shrinkage of biomass particles during devolatilization,[33] where d_b is the Sauter mean diameter of the raw biomass, Ψ is the biomass shrinkage factor, n_1 is the factor accounting for primary fragmentation of the particles, and X_c is the char conversion factor. The term $y_{s,c}$ as expressed in eq 14 describes the mass fraction of char particles in the solid fuel mixture.

$$y_{s,c} = \frac{\overline{\rho}_{s,c}}{\overline{\rho}_s}; \quad \overline{\rho}_s = \overline{\rho}_{s,c} + \overline{\rho}_{s,b} \tag{14}$$

The solid contact coefficient $\beta_{p,s}$ in eq 7 depends on the volume and particle size of the solid fuel relative to the inert bed material. Noting that the particle velocity of the bed inert material is zero, $\beta_{p,s}$ can be derived from the model given in Chang et al.[34] based on the collision theory between two different bulks of solid particles in a mixture.

$$\beta_{p,s} = \frac{3\pi(1 + e)\left(\frac{1}{2} + \frac{\mu_c\pi}{8}\right)(d_s + d_p)^2}{(\rho_p d_p^3 + \rho_s d_s^3)}\alpha_p\rho_p\overline{\rho}_s g_0|v| \tag{15}$$

$$g_0 = \frac{1}{\varepsilon_f} + \frac{3d_s d_p}{\varepsilon_f^2(d_s + d_p)}\left(\frac{\alpha_s}{d_s} + \frac{\alpha_p}{d_p}\right) \tag{16}$$

Here, $\alpha_s = \overline{\rho}_s/\rho_s$ and α_p are the solids volume fractions of the fuel particles and inert bed material, respectively. e is the coefficient of restitution between the two different particle types, μ_c is the Coulomb friction coefficient, and g_0 is their radial distribution function. ε_f is the bed voidage at the fluidized state, and d_p and ρ_p are the particle diameter and density of the inert bed material, respectively. Assuming that the momentum change of the inert bed particles as they are dragged into the bubble wake is transferred to the fuel particles within the bubble vicinity, F'_B can be modeled as

$$F'_B = -(1 - \varepsilon_{mf})\rho_p\theta_w V_B\frac{\partial u_B}{\partial z} \tag{17}$$

where ε_{mf} is the void fraction of the inert material at the minimum fluidization condition, assuming that the wake phase voidage is the same as that of the emulsion phase at this condition. θ_w is the bubble wake fraction which can be obtained depending on the inert particle diameter as reported in ref 32, and V_B is the bubble volumetric flux.

2.2.2.2. Gas Phase. For the gas phase, the interactions with the bulk of different solid materials (inert and fuel particles) as well as with the reactor walls are considered. Assuming that the fluid pressure drop over the bed is hydrostatic and that the contribution of the fuel particles on the solid mixture density is negligible, the momentum balance for the gas phase is given by

$$\frac{\partial\dot{m}''_g}{\partial t} = -\frac{\partial(\dot{m}''_g\cdot u)}{\partial z} + g[\varepsilon_f(1 - \varepsilon_f)\rho_p - \overline{\rho}_g] - \alpha_g\beta_{g,s}(-u - v) - \frac{2f_g\overline{\rho}_g}{D}u\cdot|u| - u\left(\beta_{g,p} - \sum S_{g,j}\right) - \varepsilon_f\frac{\partial p}{\partial z} \tag{18}$$

where, f_g is the wall frictional factor as given in eq 19.[35]

$$f_g = \begin{cases} \frac{16}{Re_D}; & Re_D \le 2300 \\ 0.079Re_D^{-0.25}; & Re_D > 2300 \end{cases} \tag{19}$$

$$Re_D = \frac{\rho_g D}{\mu_g}|u| \tag{20}$$

Here, Re_D is the wall Reynold number. The gas-particle momentum transfer coefficient $\beta_{g,p}$ can be obtained from different correlations.[36] For a fluid-particle drag in the dense phase ($\varepsilon_f < 0.8$), the value of $\beta_{g,p}$ can be determined from eq 21 as proposed by Gidaspow.[35]

$$\beta_{g,p} = 150\frac{\alpha_p(1 - \varepsilon_f)}{\varepsilon_f(\varphi_p d_p)^2}\mu_g + 1.75\frac{\alpha_p}{\varphi_p d_p}\rho_g|u| \tag{21}$$

Here, φ_p is the inert bed particle sphericity, μ_g is the gas dynamic viscosity, and ρ_g is the gas density as expressed in eq 22. In an incompressible flow, the gas velocity−pressure couple can be resolved numerically through the continuity equation. For simplicity, a compressible flow can be considered due to possible changes in the gas density arising from variation of mass and temperature of fluid in the reactor. The fluid pressure p is therefore modeled as in eq 23, assuming the ideal gas behavior, where R is the universal gas constant and M_g is the gas molecular weight. The pressure term in eq 18 is included to convey the mass generated in the bed appropriately along the reactor axis.

$$\rho_g = \frac{\overline{\rho}_g}{\varepsilon_f} \tag{22}$$

$$p = \frac{\rho_g RT_g}{M_g} \tag{23}$$

2.2.3. Energy Balance. The thermochemical processes in a gasifier involves exchange of heat between the gas and solids, the fuel particles and the inert bed material, the solids and the reactor walls and between the reactor walls and the environment. As gas flows through the reactor, there is a continuous heat loss. Hence, a continuous heat supply is required to keep the reactions as desired. Accounting properly the flow of heat within and across the reactor will provide a better model for predicting the reactor performance. The necessary equations proposed for solving the energy balance are detailed in the following subsections.

2.2.3.1. Solid Phase (Fuel Particles). Since the distribution of fuel particles may not be uniform due to flow of cold biomass at the inlet port and due to variation in concentration of the gasifying agent over the bed height, the sensible heat transferred by the flow of the bulk material is essential to accurately predict the heat distribution. Neglecting the contact and radiation exchange with the walls, the net heat transferred to the solid fuel

DOI: 10.1021/acs.energyfuels.9b01340
Energy Fuels 2019, 33, 7385−7397

particles in a unit volume includes the convective term due to gas flow, the collision and radiation exchange with the inert bed material and the generated heat due to reactions of the fuel particles. The distribution of the solid fuel temperature T_s over the bed height at a given time is therefore modeled by

$$\overline{\rho}_s \overline{c}_{p,s}\frac{\partial T_s}{\partial t} = -\overline{\rho}_s \overline{c}_{p,s} v\frac{\partial T_s}{\partial z} + \frac{6}{d_s}\alpha_s[h_{g,s}(T_g - T_s) + \epsilon_s \sigma(T_p^4 - T_s^4)] + h'_{p,s}(T_p - T_s) - \left(\sum r_i \Delta H^0_{ri} + r_{pyr}\Delta H^0_{pyr}\right) \quad (24)$$

where, $\overline{c}_{p,s}$ is the specific heat capacity of the solid fuel, ϵ_s is the average emissivity of the fuel particles, and σ is the Stefan–Boltzmann constant. T_p is the inert bed particle temperature and $h_{g,s}$ is the single particle convective heat transfer coefficient between the gas and the solid fuel, and it can be obtained as given in eq 25, in which Pr is the Prandl number at the gas flow condition.[37]

$$h_{g,s} = \frac{\lambda_g}{d_s}(2 + 0.6Re_s^{0.5}Pr^{0.33}) \quad (25)$$

The particle–particle heat transfer coefficient $h'_{p,s}$ per unit volume is as described in the following equations.[34]

$$h'_{p,s} = 4.88\frac{\alpha_p\alpha_s(d_s + d_p)^2}{d_s^3 d_p^3((\rho_s \overline{c}_{p,s}\lambda_s)^{-1/2} + (\rho_p \overline{c}_{p,p}\lambda_p)^{-1/2})}\left(\frac{m}{E}\right)^{3/5} (dv)^{7/10}\sqrt{8\pi(\Omega_s + \Omega_p)} \quad (26)$$

$$m = \frac{\pi}{6}\left(\frac{\rho_s\rho_p d_s^3 d_p^3}{\rho_s d_s^3 + \rho_p d_p^3}\right) \quad (27)$$

$$E = \frac{4/3}{\frac{(1-\nu_s^2)}{G_s} + \frac{(1-\nu_p^2)}{G_p}}; \quad d = \frac{d_s d_p}{2(d_s + d_p)} \quad (28)$$

$$\Omega_s = \frac{2(u - v_{t,s})^2}{15(1-e)}\left(\frac{d_s}{D}\right)^2; \quad \Omega_p = \frac{2(u - v_{t,p})^2}{15(1-e)}\left(\frac{d_p}{D}\right)^2 \quad (29)$$

Here, $v_{t,s}$ is the terminal velocity of the solid fuel particles and $v_{t,p}$ is the corresponding value for the inert material. λ_s and λ_p are their respective thermal conductivity, and Ω_s and Ω_p the corresponding granular temperatures. While ν_s and ν_p are the Poison's ratios, G_s [GPa] and G_p [GPa] are the Young's modulus of the different particle types. The last term in eq 24 is the net heat generated during the conversion of the fuel particles in the heterogeneous reactions (i = 5, 6, 7) and in the devolatilization (pyrolysis) stage, where $r_{pyr} = \overline{\rho}_{s,b}\sum k_i$.

2.2.3.2. Gas Phase. For the gas phase, the heat balance also includes the convective heat exchange with the inert bed material due to a possible temperature difference between the two media. Assuming that the reactor walls are in thermal equilibrium with the gas, the energy balance is thus given by

$$\overline{\rho}_g \overline{c}_{p,g}\frac{\partial T_g}{\partial t} = -\overline{\rho}_g \overline{c}_{p,g} u\frac{\partial T_g}{\partial z} - \frac{6}{d_s}\alpha_s h_{g,s}(T_g - T_s) - \frac{6}{\varphi_p d_p}\alpha_p h_{g,p}(T_g - T_p) - \frac{4}{D}U_a(T_g - T_a) - \sum (r_i \Delta H^0_{r,i}) \quad (30)$$

where, $\overline{c}_{p,g}$ is the gas specific heat capacity and U_a is the overall heat transfer coefficient between the gas and the surroundings at ambient temperature T_a through the reactor walls. The last term in eq 30 includes only the homogeneous reactions (i = 8, 9 in Table 3). The convective heat transfer coefficient $h_{g,p}$ between the gas and inert bed material in fluidized state can be obtained as descried below.[38]

$$h_{g,p} = \frac{\lambda_g}{d_p}[(7 - 10\varepsilon_f + 5{\varepsilon_f}^2)(1 + 0.7Re_p^{0.2}Pr^{0.33}) + (1.33 - 2.4\varepsilon_f + 1.2{\varepsilon_f}^2)Re_p^{0.7}Pr^{0.33}] \quad (31)$$

$$Re_p = \frac{\rho_g d_p}{\mu_g}|u| \quad (32)$$

2.2.3.3. Solid Phase (Inert Bed Particles). With the assumption that the mean velocity of the inert particles is zero, T_p can be obtained from eq 33, where $\overline{c}_{p,p}$ is the specific heat capacity of the inert bed material.

$$\alpha_p\rho_p \overline{c}_{p,p}\frac{\partial T_p}{\partial t} = \frac{6}{\varphi_p d_p}\alpha_p h_{g,p}(T_g - T_p) - \frac{6}{d_s}\alpha_s\epsilon_s \sigma(T_p^4 - T_s^4) - h'_{p,s}(T_p - T_s) + K_r\sigma(T_w^4 - T_p^4) + \frac{4}{D}\alpha_p h_{w,p}(T_w - T_p) \quad (33)$$

Here, $T_w = T_g$ is the wall temperature under the gas-wall thermal equilibrium. Assuming that the bulk inert material is a cylinder concentric with the reactor walls (cylinder), eq 34 can be derived for the effective radiation coefficient K_r, where ϵ_p and ϵ_w are the emissivity of the inert particle and the reactor wall materials, respectively.

$$K_r = \frac{4}{D}\left[\frac{1 - \epsilon_p}{\epsilon_p{\alpha_p}^2} + \frac{1}{\epsilon_w}\right]^{-1} \quad (34)$$

The heat transfer coefficient $h_{w,p}$ between the bulk inert particles and the reactor walls due to the combined cluster convection and gas-gap conduction can be evaluated as described in the Supporting Information.

2.2.4. Bubble Properties and Bed Expansion. The gasification model outlined in the previous section requires accurate prediction of the bubble properties (diameter, volumetric flux, and bubble velocities) and bed expansion. There are several models for predicting the bubble diameter and bubble velocity.[39] The most common methods for prediction of bubble volumetric flux V_B and bed voidage ε_f at fluidized state are those based on the two-phase theory as described in Kunii and Levenspiel.[32] The inaccuracy in predicting the bed voidage and expansion can affect the model global accuracy. A higher bed voidage indicates flow of faster and larger bubbles as well as a lower gas–solid contact time due to a reduced gas residence

DOI: 10.1021/acs.energyfuels.9b01340
Energy Fuels 2019, 33, 7385–7397

time. On the other hand, the distributions of heat and materials will be poor when the bed is not well expanded. For the particles exhibiting Geldart B behavior at ambient conditions, the bubble velocity u_B, the bed voidage (with the bed expansion $\Delta e = (l_f - l_0)/l_0$) and the bubble volumetric flux can be computed using the correlations[40,41] given in eqs 35−39.

$$u_B = 12.51(u_{sf} - u_{mf})^{0.362}\left(\frac{d_B}{D}\right)^{0.52} D \tag{35}$$

$$\Delta e = \left[1 - 0.103(u_{sf} - u_{mf})^{-0.362}\left(\frac{\overline{d}_B}{D}\right)\right]^{-1} - 1 \tag{36}$$

$$\varepsilon_f = 1 - \frac{1 - \varepsilon_{mf}}{1 + \Delta e} \tag{37}$$

$$l_f = \frac{1 - \varepsilon_0}{1 - \varepsilon_f} l_0 \tag{38}$$

$$V_B = 1.285\left(\frac{d_B}{D}\right)^{1.52} D \tag{39}$$

Here, u_{sf} is the superficial gas velocity at the inlet boundary condition, u_{mf} is the particle minimum fluidization velocity, d_B is the bubble diameter at any position z along the bed axis, and $\overline{d}_B$ is the bubble diameter averaged over the bed height which can be obtained by integrating the bubble diameter d_B within the interval $[0, l_f]$ from the distributor. ε_0 and l_0 are the voidage and bed height at fixed state, respectively. With the value of the bed height l_f, the freeboard region $L - l_f$ is defined, and based on the value of ε_f, the conservation of the bed inventory is obtained as

$$\alpha_p + \alpha_s = 1 - \varepsilon_f \tag{40}$$

While the bubble diameter depends on the bed particles, it is also affected by temperature. For fine particles, the bubble diameter decreases with increasing temperature.[32] However, most of the available models for bubble diameter give the opposite trend at a given value of u_{sf} since u_{mf} decreases with increasing temperature. The correlation proposed by Agu et al.[41] for predicting the average bubble diameter over the bed height can account for the effects of particle and fluid properties, but it is limited to only large particles for which the Archimedes number >400. Nevertheless, to close the proposed gasifier model, the values of d_B can be evaluated based on the Werther[42] correlation as given in eq 41 while the other correlations required to completely solve the balance equations are reported in Table 4.

$$d_B = 0.00853[1 + 27.2(u_{sf} - u_{mf})]^{1/3}(1 + 6.84z)^{1.21} \tag{41}$$

In Table 4, M_j is the molecular weight of the gas species, x_j is the gas mole fraction, and n is the number of species in the gas phase. The specific heat capacity $\overline{c}_p$, dynamic viscosity μ, and thermal conductivity λ of each gas species are correlated with temperature as documented in the work of Coker.[43] The gas mixture viscosity and thermal conductivity are obtained by the Wilke[44] mixing rules whereas other properties are based on the linear mixing rule. The correlation of $\overline{c}_p$ with temperature for biomass and char particles can also be obtained from literature[24] as described in the Supporting Information.

Table 4. Algebraic Equations and Mixing Rules for Different Mixtures

expressions	units
$\overline{c}_{p,k} = \sum y_j \overline{c}_{pj} \quad k \in (s, g)$	J/(kg·K)
$M_g = \sum x_j M_j$	kg/kmol
$x_j = \frac{y_j}{M_j \sum\left(\frac{y_j}{M_j}\right)}$	
$\mu_g = \sum_{J=1}^{n}\left(\frac{x_J \mu_J}{\sum_{j=1}^{n} x_j \varnothing_{Jj}}\right)$	Pa·s
$\lambda_g = \sum_{J=1}^{n}\left(\frac{x_J \lambda_J}{\sum_{j=1}^{n} x_j \varnothing_{Jj}}\right)$	W/(m·K)
$\varnothing_{Jj} = \frac{\left[1 + \left(\frac{\mu_J}{\mu_j}\right)^{0.5}\left(\frac{M_j}{M_J}\right)^{0.25}\right]^2}{\sqrt{8\left(1 + \frac{M_J}{M_j}\right)}}$	
$Pr = \frac{\overline{c}_{pg}\mu_g}{\lambda_g}$	

[a] j or J is the species in the respective phase k (solids or gas).

3. MODEL NUMERICAL SOLUTION

The set of nonlinear partial differential equations proposed for a gasification process can be discretized into a number of ordinary differential equations using the finite volume method. Like many other numerical solutions, the grid size and size distribution affect the accuracy of the model; the finer the grid, the better the solution but the longer the computational time. For the present study, the gasifier model is discretized into 110 grid points along the reactor axis comprising 80 grid points within the bed (50 below the biomass feeding position and 30 above) and 30 grid points in the freeboard to ensure that the numerical solution is closer to the possible analytical solution. The grid point lies at the center of the computational cell of height Δz as shown in Figure 2b. All the scalar quantities including the bulk density and temperature of different phases are computed at the grid points whereas the mass flux or gas velocity is evaluated and stored at the cell faces so that information from one cell to another can be conveyed. The fuel particle velocity is also computed at the cell center due to the nonconservative nature of the governing equation. The resulting equations are solved in MATLAB using the ode 23tb solver with an adaptive time-step. The inlet gas flow is given at the bottom of the bed while the zero pressure gradient is defined at the exit as shown in Figure 2a. The model stability depends on the treatment of the internal boundary where the biomass feed is located and on the interface boundary between the bed and the freeboard due to the coupling effect between the gas momentum and continuity equations. The treatment of boundary condition at the biomass feeding position is described in the Supporting Information.

For all the results presented, the computation of the kinetic rate constants for the pyrolysis is at the solid fuel temperature T_s while that for the different heterogeneous reactions are at the film temperature, $\overline{T}_s = 1/2(T_s + T_g)$ since gasification takes place on the surface of the fuel particles. For estimation of bubble properties, the superficial gas velocity computed as $u_{sf} = \frac{1}{N}\varepsilon_f \sum_{I=1}^{N}(u_I)$ is applied, where u_I is the gas velocity

DOI: 10.1021/acs.energyfuels.9b01340
Energy Fuels 2019, 33, 7385−7397

computed at each cell face I and N is the total number of grid points within the bed. The steady state solution of the model depends on a combination of different factors including the bed temperature, feed rate, particle properties, and the position in the reactor. To achieve a steady state at a given operating condition, where the bed containing inert particles is initially free of the fuel particles (biomass and char) and the available void space is filled with only steam at the gasification temperature, each simulation was run for 3×10^4 s. Thus, all the results reported in this paper were obtained at the end of this simulation time.

4. MODEL VALIDATION

The model results are compared with the experimental data in the literature to ascertain its accuracy. Based on biomass gasification with steam, the data presented in Li et al.[45] and Gopalakrishnan[14] are used. Both studies were conducted using two different dual fluidized bed reactors. In the work of Li et al.,[45] the diameter of the gasifier is 0.28 m and the bed contained 120 kg silica sand of mean particle size 143 μm, initially loaded to a height of 1.27 m. For each operating temperature in the range 690−830 °C, softwood pellets were applied at a feed rate of 10 kg/h and steam at a flow rate of 10 kg/h. The gasifier in the Gopalakrishnan[14] study was rated 100 kW at a biomass feed rate of 15 kg/h using sawdust pellets as the feedstock. The biomass was fed at a position 0.2 m above the distributor. The 0.2 m diameter column contained greywacke sand particles with a mean size of 275 μm and an initial height of 0.24 m.

These two reactors have also been modeled in different studies as can be found in the work of Hejazi et al.[16] and Gopalakrishnan.[14] Both reactor models are one-dimensional and were developed based on the two-phase theory. The experimental data from these two reactors can therefore be used to compare the performance of the proposed model with the existing ones.[14,16] The proposed model results are also compared with the simulated results from a 2D hydrodynamic model also outlined in ref 14.

The biomass feeding position in the Li et al.[45] study is not clearly defined, but it is well inside the bed. For the preliminary model validation, l_{sb} = 0.63 m is assumed. The effect of biomass feeding position will be further discussed based on this gasifier.

In a steam biomass gasifier, the operation can be controlled to maintain the same bed temperature by circulating the inert particles through a fluidized bed combustor. More often, the gasifier operating temperature is the same as the temperature of the incoming superheated steam, leading to an isothermal process. It should be noted that the model developed in this study does not include circulation of the bed material. Therefore, the heat flow into the gasifier as accounted by the current model is from the incoming steam and the possible exothermic reactions in the bed, giving room for a non-isothermal process. To achieve an isothermal behavior, the bed temperature is assumed the same as the temperature of the incoming steam in the simulations. In later discussions, the nonisothermal behavior of the model is compared with the behavior under isothermal condition for evaluation of the amount of energy required to achieve a desired operating temperature.

Figure 3a shows the composition of the product gas obtained from the experimental setup of Gopalakrishnan[14] at 780 °C and the steam-biomass ratio (S/B) of 0.53 (7.95 kg/h steam flow rate). In the figure, the predictions based on the present model are compared with the experimental data and also with those

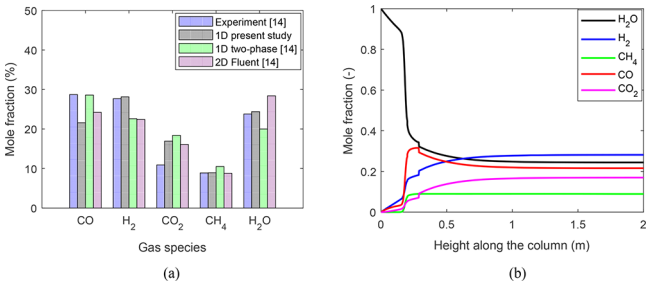

Figure 3. Predicted gas composition at 780 °C and S/B = 0.53 (a) compared with experimental data and with results from existing models[14] (b) showing the axial distribution of the gas species based on the present model.

based on the 1D and 2D models presented in Gopalakrishnan.[14] As can be seen, the results from the three models agree reasonably well with the experimental data. With the proposed model, the agreement is better for the H_2, CH_4, and H_2O mole fractions. For the mole fractions of CO and CO_2, the predictions from the present model are closer to those of the 2D model, which gives a better prediction of CH_4 than the Gopalakrishnan[14] 1D model. The predicted distribution of the gas species along the bed axis, as shown in Figure 3b, is also in agreement with that given by the 2D model[14] (see Figure 6.16(a) in ref 14). Figure 3a also shows that the present model predicts the sum of the mole fractions of H_2 and H_2O in a good agreement with the experiment (2% error), which is also true for the sum of CO and CO_2 (−2% error). However, the Gopalakrishnan[14] 1D model over predicts the $(CO + CO_2)$ value by 19% and under predicts that of $(H_2 + H_2O)$ by 17%. With the 2D model, the predictions of the different sums are also closer to the experiment, where the error for the $(CO + CO_2)$ value is 2% and that for the $(H_2 + H_2O)$ value is −1%. These results thus show that the proposed model can predict the gas yields obtained from an experiment quite well.

Figure 4 compares the gas composition predicted at different temperatures with the experimental data from Li et al.[45] Above 690 °C, the model results agree quite well with the experiments, especially for the CH_4 and CO_2 mole fractions. The scattered behavior of the experimental data is due to variation of the steam-biomass ratio in the range 0.94−1.05 as noted in the literature.[45] Comparing with the results from the 1D model presented in Hejazi et al.[16] (see Figure 5 and Table 7 in ref 16), the present model has a better prediction accuracy for the experimental data. Based on the present study, the mean absolute errors over the temperature range of the experiments shown in Figure 4 are 11, 7, 10, and 9% for H_2, CO, CO_2, and CH_4, respectively; whereas the corresponding values are 67, 40, 17, and 72% based on the Hejazi et al.[16] 1D model.

5. DISCUSSION

Since the accuracy of the proposed model is reasonably good, the model can be used to investigate different operating parameters and design choices on the gasification behavior. In this study, the effect of biomass feeding position on the gas composition and that of temperature on the total gas yield are discussed using the gasifier described in Li et al.[45] as a case study. In addition, a comparison between the isothermal and nonisothermal modes of operation is discussed.

5.1. Effect of Biomass Feeding Position on the Gas Composition. The gas compositions predicted at different biomass feeding positions are shown in Figure 5. In the result,

DOI: 10.1021/acs.energyfuels.9b01340
Energy Fuels 2019, 33, 7385−7397

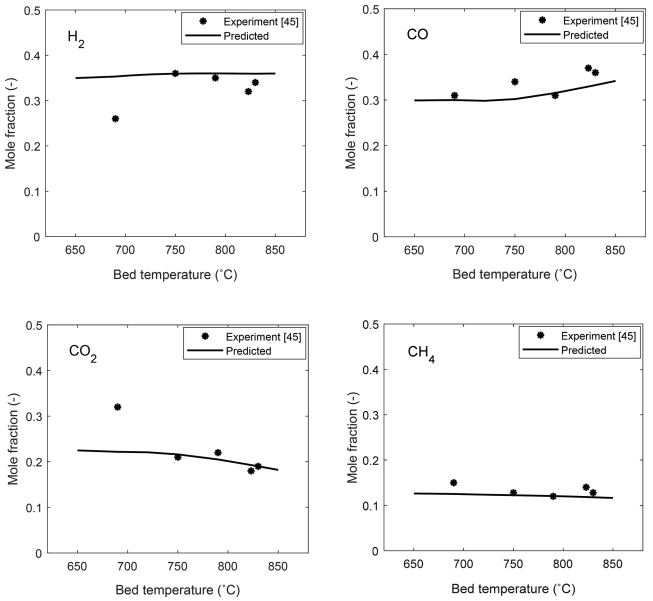

Figure 4. Predicted gas composition (dry basis) compared with experimental data[45] (l_{sb} = 0.63 m, S/B = 1.0) at different bed temperatures.

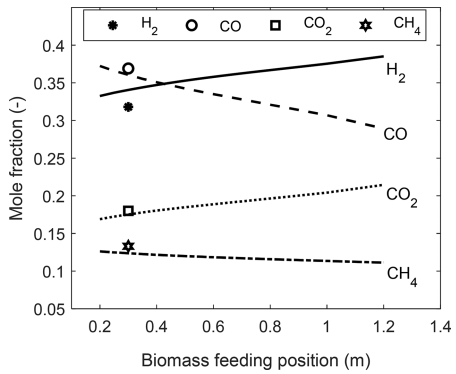

Figure 5. Predicted gas composition, showing the effect of biomass feeding position on gasification behavior. S/B = 1.0 and T = 830 °C: data points = experiment,[45] lines = predicted values.

the distribution of the grid points along the reactor column is kept constant for all the biomass-feeding points. The figure shows that moving the feeding position toward the bed surface increases the amounts of H_2 and CO_2 and decreases those of CO and CH_4 in the product gas. With biomass fed close to the bottom of the bed, char conversion through reaction route 5 in Table 3 is favored due to higher availability of steam and char particles as well as their increased contact time. This leads to a reduced amount of H_2O available for the freeboard reactions, thereby reducing the yields of H_2 and CO_2. Supplying biomass near the bed surface leads to a lower char conversion and a higher availability of H_2O in the freeboard. The exothermic water gas shift dominates the process, leading to higher H_2 and CO_2 concentrations. The steam-methane reaction is also enhanced, resulting in a decrease in the CH_4 mole fraction. Moreover, due to the low density of the char particles, their poor sinking behavior into the bed also influences the poor conversion of the fuel particles at increasing biomass-feeding position. Lowering the feeding position to about 0.3 m, Figure 5 shows that the predicted gas composition is consistent with the experimental data reported at about 830 °C.[45] The trends of the results in Figure 5 are also similar to those observed by Radmanesh et al.[15] whose experimental data were compared with data from Narvaez et al.[46] However, the 1D two-phase model presented in ref 15 showed poor predictions of CO and H_2 compared to the experimental data[46] obtained when the biomass is fed close to the bottom of the bed.

5.2. Effect of Temperature on the Total Gas Yield. In addition to the product gas composition, an important output from the proposed model is the cold gas production rate (gas yield), Y, determined from the following equation.

$$Y = \frac{\pi D^2}{4} \frac{(1 - x_{\mathrm{H2O}})}{\dot{m}_{b,\mathrm{in}}(1 - y_{\mathrm{moist}})} \left(\frac{T_{\mathrm{std}}}{T_g}\right)\left(\frac{\dot{m}_g''}{\overline{\rho}_g}\right) \tag{42}$$

Here, T_{std} = 273.15 K is the standard temperature and y_{moist} is the weight fraction of moisture in the raw biomass. The term $\dot{m}_g''/\overline{\rho}_g$ is the gas velocity evaluated at the gas exit temperature T_g, and x_{H2O} is the mole fraction of water in the product gas. As shown in Figure 6a, the gas velocity increases with an increase in the

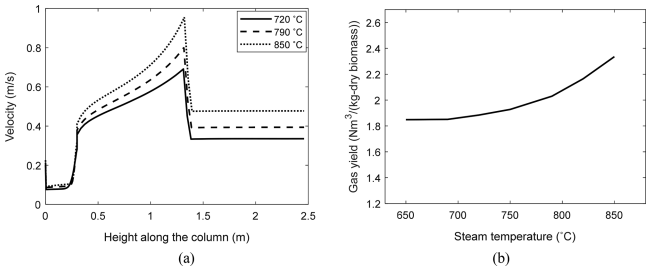

Figure 6. Predicted (a) gas velocities and (b) total gas yield on a dry basis at different temperatures based on the gasifier described in ref 45. S/B = 1.0, l_{sb} = 0.3 m.

temperature due to increasing amount of pyrolysis gas above the biomass feeding position. Above the bed surface, the velocity decreases to a constant value as the gas bulk density is increased in the absence of solid particles. In practice, the high gas velocity at the bed surface would result in splash of particles into the freeboard. However, as this splash zone and particle entrainment are not considered in the developed model (cf. section 2.2.2), the decrease in the gas velocity is relatively sharp. The profile of the gas velocity could have been improved by properly accounting for the bed−freeboard interface conditions. One possibility is to calculate the splash zone height based on the momentum balance of the solids carried in the wake of erupting bubbles.

Figure 6b shows that the gas yield increases with increasing temperature owing to the increase in the conversions as well as the gas specific volume. The value of Y predicted is comparable with those obtained from the thermodynamic equilibrium model and from the experiments,[47] which although is difficult to be measured. As expected, the value of Y predicted at 830 °C is higher than the experimental value of 1.03 N m^3/kg-dry biomass reported in the literature.[45] In the model predictions, all the char particles are available for the gasification reactions, leading to a higher gas yield. In the experimental reactor, some of the char particles are burned off in the combustor while some are entrained from the reactor, resulting in a lower gas yield. The predicted gas yield is also in agreement with the yield measured when biomass is gasified with air/oxygen in a bubbling bed where there is a lower char loss in the absence of bed material circulation.[48]

DOI: 10.1021/acs.energyfuels.9b01340
Energy Fuels 2019, 33, 7385−7397

5.3. Comparison between Isothermal and Nonisothermal Operations. In an isothermal gasification process, the temperature of the inert bed material is the same as that of the incoming steam whereas the two temperatures differ in the nonisothermal case. This means that, in the isothermal operation where $T_p = T_g$, eq 33 is not required in the simulation. To simulate the gasification process under the nonisothermal condition, eq 33 is applied in addition to energy equations described in section 2.2.3 for the fuel particles and gas phase. The performance of the gasifier[45] under the two different modes of operations are compared in this section.

5.3.1. Temperature Distribution. Figure 7a compares the axial temperature distribution for the two different modes of

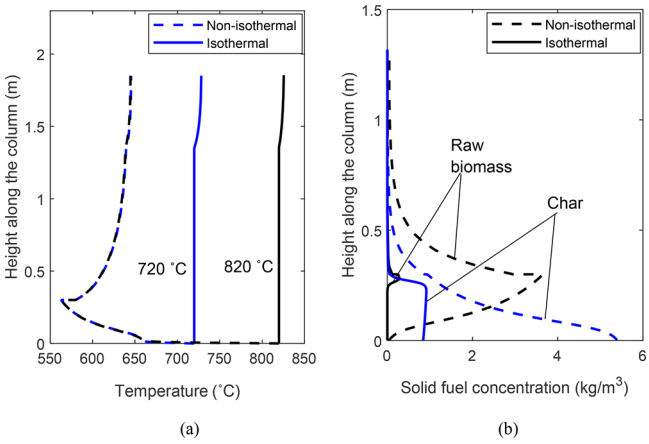

Figure 7. Predicted axial (a) temperature distribution and (b) concentration of the solid fuel species, comparing isothermal and nonisothermal gasification processes at different steam temperatures; l_{sb} = 0.3 m, S/B = 1.0.

operation. Under the isothermal operation, the gas temperature is the same over the bed height but slightly increases in the freeboard due to the exothermic water−gas shift (WGS) reaction. However, the distribution of temperature in the nonisothermal condition is independent of the incoming steam temperature within 720−820 °C. The gas temperature decreases toward the biomass feeding position due to flow of cold biomass into the bed. Above the feeding point, the exothermic activities increase the temperature to an equilibrium value. The difference in temperature between the isothermal and nonisothermal processes therefore gives an indication about how much heat is required to main the gasification at a given operating condition. Moreover, the temperature remains high over the length of the freeboard in both operations as the heat loss is neglected in the simulations. In practice, however, the gas temperature may be lower and may also decrease along the freeboard due to heat loss and possibly significant endothermic reactions.

The temperature distribution also influences the distributions of raw biomass and char in the bed as shown in Figure 7b. Due to the high temperature, biomass particles rapidly undergo devolatilization before reaching the bottom of the bed in the isothermal condition. The high bed temperature also enhances the char conversion, resulting in a lower char accumulation compared to the nonisothermal case. As the temperature is low to enhance devolatilization, the figure also shows that higher amount of biomass than char is accumulated in the bed in the nonisothermal process. Comparing with results reported in literature, both the temperature and biomass concentration profiles under nonisothermal conditions are similar than those presented in the work of Xue and Fox,[49] although the flow of the fuel particles up the bed is not well captured in the current model simulation. The distribution of biomass and char can be enhanced by improving interactions of the solid fuel particles with gas and inert bed material in the developed model.

5.3.2. Distribution of Gas Species. Figure 8 shows that the conversion of steam in the bed increases with increasing

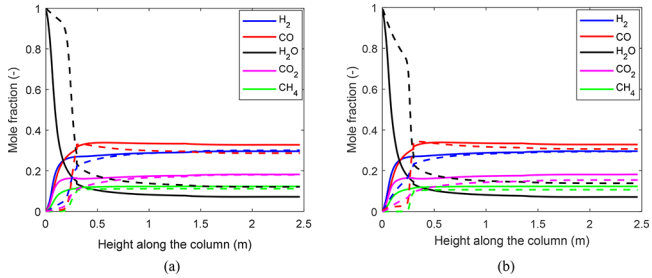

Figure 8. Predicted axial distribution of gas species (l_{sb} = 0.3 m, S/B = 1.0), comparing isothermal (dashed line) and nonisothermal (solid line) gasification processes at different temperatures T = (a) 720 and (b) 820 °C.

temperature under the isothermal condition owing to the higher temperature shown in Figure 7a. The difference in the gas composition between the two processes is more pronounced in the bed but diminishes in the freeboard as the temperature is increased, particularly for CO concentration. The higher CO_2 concentration compared to CO as can be clearly seen in Figure 8b indicates that the WGS reaction is also favored in the lower part of the bed in isothermal operation. Above the feeding position, the WGS reaction dominates the isothermal process. The mole fraction of CO decreases below the value in the bed while the mole fractions of H_2 and CO_2 increase significantly. The concentration of hydrogen in the freeboard is invariant between the two processes due to the influence of the equilibrium WGS reaction, and the variation of methane suggests that the reaction of the species with steam increases with increasing temperature. Moreover, the CH_4 yield below the feeding position in the isothermal operation is negligible because biomass devolatilization is complete before the bottom of the bed in addition that the reaction between char with H_2 is very slow. In the nonisothermal process, all the permanent gas species are present in the bottom of the bed due to accumulation of the raw biomass as shown in Figure 7b. Moreover, the distribution of gas species is almost uniform shortly above the point of biomass introduction, suggesting that the gas yield and composition attain equilibrium conditions in the nonisothermal process.

5.3.3. Product Gas Composition at Different Temperatures. As the reactions tend toward the equilibrium condition, Figure 9 shows that there is no significant difference in the product gas composition at different temperatures when the process is operated in the nonisothermal mode. However, in the isothermal mode, the gas composition varies significantly with changes in the bed temperature. The amounts of H_2 and CO_2 decrease with an increase in temperature under this condition. The increasing CO and H_2O mole fractions suggest that the WGS reaction is less favored as the temperature is increased. As there is no absolute isothermal condition in reality, a slightly lower congruence as presented in Figure 9 should be expected.

DOI: 10.1021/acs.energyfuels.9b01340
Energy Fuels 2019, 33, 7385−7397

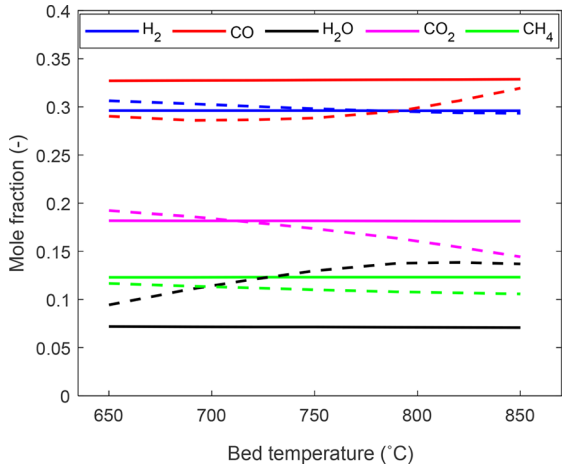

Figure 9. Product gas composition (l_{sb} = 0.3 m, S/B = 1.0), comparing isothermal (dashed line) and nonisothermal (solid line) gasification processes at different steam temperatures.

6. CONCLUSIONS

A model for simulating a bubbling fluidized bed gasifier was developed. The model includes the momentum equations of fluid and fuel particles to account for the effect of bed material properties on the flow behavior. The proposed one-dimensional unsteady state model was used to investigate the performance of steam gasifiers with different biomass feeding positions and different modes of operation (isothermal and nonisothermal processes with respect to steam temperature and gasifier temperature).

The results show that the model can predict the total gas production rate depending on the reactor design and operating conditions. Increasing the biomass feeding position toward the bed surface decreases the CO mole fraction and increases that of H_2 in the product gas due to a reduced char conversion effect and an enhanced water gas shift reaction.

The proposed model can be applied to any bubbling fluidized bed reactor, and it is computationally less demanding, thus can be used to improve the design and operational control. The model can be developed further to include circulation of inert bed material and integration with a circulating fluidized bed combustor. Future studies will also include sensitivity and uncertainty analyses of different inputs and further validation of the proposed model with different experimental data.

■ ASSOCIATED CONTENT

Supporting Information

The Supporting Information is available free of charge on the ACS Publications website at DOI: 10.1021/acs.energyfuels.9b01340.

Details on average bed density, convective heat transfer coefficient, correlations for different gas species, Tables S1−S6, and Figure S1 (PDF)

■ AUTHOR INFORMATION

Corresponding Author

*Email: cornelius.e.agu@usn.no.

ORCID

Cornelius E. Agu: 0000-0002-5339-9794

Christoph Pfeifer: 0000-0002-7747-9297

Notes

The authors declare no competing financial interest.

■ NOMENCLATURE

Symbols

A [1/s] = frequency factor
a [−] = fitting index
c [K^{-a}] = fitting coefficient
C_d [−] = drag coefficient
$\overline{c}_p$ [J/kg K] = specific heat capacity
D [m] = vessel diameter
D_R [N s/m] = drag resistance
d [m] = diameter
$\overline{d}$ [m] = height-averaged diameter
E [J/mol] = activation energy
e [−] = coefficient of restitution
Δe [−] = bed expansion
F [N] = force
F' [N/m^3] = force per unit volume
f [−] = friction factor
G [GPa] = Young's modulus
g [m/s^2] = acceleration due to gravity
g_0 [−] = radial distribution function
ΔH_r^0 [J/kg] = reaction enthalpy change
h [W/m^2 K] = unit area heat transfer coefficient
h' [W/m^3 K] = unit volume heat transfer coefficient
K_r [1/m] = effective radiation coefficient
k [1/s] = rate constant
L [m] = total column height
l [m] = height above bed base
l_{sb} [m] = biomass feeding height
M [kg/kmol] = molecular weight
$\dot{m}$ [kg/s] = mass flow rate
$\dot{m}_{b,in}$ [kg/s] = biomass feed rate
$\dot{m}''$ [kg/s m^2] = mass flux
N and n [−] = number
n_1 [−] = fragmentation factor
Pr [−] = Prandtl number
p [Pa] = fluid pressure
R [J/mol K] = universal gas constant
r [mol/m^3 s] = reaction rate constant
Re [−] = Reynolds number
S [kg/m^3 s] = mass generation rate
T [K] = temperature
T_{std} [K] = temperature at standard condition
t [s] = time
U [W/m^2 K] = overall heat transfer coefficient
u [m/s] = gas velocity
u_{sf} [m/s] = superficial gas velocity
V_B [m/s] = bubble volumetric flux
v [m/s] = fuel particle velocity
v_t [m/s] = particle terminal velocity
X_c [−] = char conversion factor
x [−] = mole fraction
x_{H2O} [−] = mole fraction of water in product gas
Y [N m^3/kg] = cold gas yield
y [−] = mass fraction
y_{moist} [−] = mass fraction of biomass moisture content
z [m] = axial position
Δz [m] = computational grid size

Greek Letters

α [−] = solids volume fraction

DOI: 10.1021/acs.energyfuels.9b01340
Energy Fuels 2019, 33, 7385−7397

β [N s/m^4] = momentum transfer coefficient
ϵ [−] = emissivity
ε [−] = void fraction
Ω [m^2/s^2] = granular temperature
Λ [−] = uncorrected pyrolysis gas mole fraction
λ [W/m K] = thermal conductivity
σ [W/m^2 K^4] = Stefan−Boltzmann constant
ρ [kg/m^3] = density
$\overline{\rho}$ [kg/m^3] = mass concentration
θ_w [−] = bubble wake fraction
ν [−] = Poison's ratio
ϑ [−] = pyrolysis gas mole fraction
μ [Pa s] = dynamic viscosity
μ_c [−] = Coulomb friction coefficient
Ψ [−] = shrinkage factor
$\varnothing$ [−] = interaction parameter
φ [−] = particle sphericity
γ [−] = mass fraction of tar components

Subscripts

a = ambient
B = bubble
b = biomass
c = char
f = fluidized state
g = gas
I, i = step
J, j = species
k = phase
m = mixture
mf = minimum fluidization
p = inert particle
r = reaction
s = solid fuel
w = wall
0 = initial

Abbreviations

S/B = mass of steam to mass of biomass ratio
WGS = water−gas shift
1D = one-dimensional
2D = two-dimensional
3D = three-dimensional

REFERENCES

(1) Chen, J.; Yu, G.; Dai, B.; Liu, D.; Zhao, L. CFD simulation using a bubble-based drag model. *Energy Fuels* **2014**, *28*, 6351.
(2) Chen, J.; Yin, W.; Wang, S.; Yu, G.; Li, J.; Hu, T.; Lin, F. Modelling of coal/biomass co-gasification in internal circulating fluidized bed using kinetic theory of granular mixture. *Energy Convers. Manage.* **2017**, *148*, 506.
(3) Liu, H.; Elkamel, A.; Lohi, A.; Biglari, M. Computational fluid dynamics modeling of biomass gasification in circulating fluidized-bed reactor using the Eulerian-Eulerian approach. *Ind. Eng. Chem. Res.* **2013**, *52*, 18162.
(4) Gao, X.; Zhang, Y.; Li, B.; Yu, X. Model development for biomass gasification in an entrained flow gasifier using intrinsic reaction rate submodel. *Energy Convers. Manage.* **2016**, *108*, 120.
(5) Gonzalez-Vazquez, P. M.; Garcia, R.; Pevida, C.; Rubiera, F. Optimization of a bubbling fluidized bed plant for low-temperature gasification of biomass. *Energies* **2017**, *10*, 306.
(6) Mazaheri, N.; Akbarzadeh, A. H.; Madadian, E.; Lefsrud, M. Systematic review of research guidelines for numerical simulation of biomass gasification for bioenergy production. *Energy Convers. Manage.* **2019**, *183*, 671.
(7) Mahishi, M. R.; Goswami, D. Y. Thermodynamic optimization of biomass gasifier for hydrogen production. *Int. J. Hydrogen Energy* **2007**, *32*, 3831.
(8) Pauls, J. H.; Mahinpey, N.; Mostafavi, E. Simulation of air-steam gasification of woody biomass in a bubbling fluidized bed using Aspen Plus: A comprehensive model including pyrolysis, hydrodynamics and tar production. *Biomass Bioenergy* **2016**, *95*, 157.
(9) Liu, H.; Elkamel, A.; Lohi, A.; Biglari, M. Computational fluid dynamics modeling of biomass gasification in circulating fluidized-bed reactor using the Eulerian−Eulerian approach. *Ind. Eng. Chem. Res.* **2013**, *52*, 18162.
(10) Ku, X.; Li, T.; Løvås, T. CFD-DEM simulation of biomass gasification with steam in a fluidized bed reactor. *Chem. Eng. Sci.* **2015**, *122*, 270.
(11) Chen, C.; Werther, J.; Heinrich, S.; Qi, H.-Y.; Hartge, E.-U. CPFD simulation of circulating fluidized bed risers. *Powder Technol.* **2013**, *235*, 238.
(12) Thapa, R. K.; Pfeifer, C.; Halvorsen, B. M. Modeling of reaction kinetics in bubbling fluidized bed biomass gasification reactor. *Int. J. Energy Environ.* **2014**, *5*, 35.
(13) Gungor, A.; Yildirim, U. Two dimensional numerical computation of a circulating fluidized bed biomass gasifier. *Comput. Chem. Eng.* **2013**, *48*, 234.
(14) Gopalakrishnan, P. Modelling of biomass steam gasification in a bubbling fluidized bed gasifier. PhD. Thesis, The University of Canterbury, 2013.
(15) Radmanesh, R.; Chaouki, J.; Guy, C. Biomass gasification in a bubbling fluidized bed reactor: Experiments and modeling. *AIChE J.* **2006**, *52*, 4258.
(16) Hejazi, B.; Grace, J. R.; Bi, X.; Mahecha-Botero, A. Kinetic model of steam gasification of biomass in a dual fluidized bed reactor: Comparison with pilot-plant experimental results. *Energy Fuels* **2017**, *31*, 12141.
(17) Toomey, R. D.; Johnstone, H. F. Gaseous fluidization of solid particles. *Chem. Eng. Prog.* **1952**, *48*, 220.
(18) Inayat, A.; Ahmad, M. M.; Yusup, S.; Mutalib, M. I. A. Biomass steam gasification with in-situ CO_2 capture for enriched hydrogen gas production: A reaction kinetics modelling approach. *Energies* **2010**, *3*, 1472.
(19) Solsvik, J.; Chao, Z.; Jakobsen, H. A. Modeling and simulation of bubbling fluidized bed reactors using a dynamic one-dimensional two-fluid model: The sorption-enhanced steam methane reforming process. *Adv. Eng. Softw.* **2015**, *80*, 156.
(20) Silva, J. D. Numerical modelling of the fluid dynamics in a bubbling fluidized bed biomass gasifier. *J. Petroleum Gas Eng.* **2012**, *3*, 35.
(21) Miccio, F. Modeling percolative fragmentation during conversion of entrained char particles. *Korean J. Chem. Eng.* **2004**, *21*, 404.
(22) Agu, C. E.; Tokheim, L.-A.; Pfeifer, C.; Moldestad, B. M. E. Behaviour of biomass particles in a bubbling fluidized bed: A comparison between wood pellets and wood chips. *Chem. Eng. J.* **2019**, *363*, 84.
(23) Salatino, P.; Solimene, R. Mixing and segregation in fluidized bed thermochemical conversion of biomass. *Powder Technol.* **2017**, *316*, 29.
(24) Basu, P. *Biomass Gasification, Pyrolysis, and Torrefaction−Practical Design and Theory*, second ed.; Elsevier Inc., London, UK, 2013.
(25) Shafizadeh, F.; Chin, P. P. S. Thermal deterioration of wood. *ACS Symp. Ser.* **1977**, *43*, 57.
(26) Chan, W-C. R.; Kelbon, M.; Krieger, B. B. Modelling and experimental verification of physical and chemical processes during pyrolysis of a large biomass particle. *Fuel* **1985**, *64*, 1505.
(27) Matsui, I.; Kunii, D.; Furusawa, T. Study of fluidized bed steam gasification of char by thermogravimetrically obtained kinetics. *J. Chem. Eng. Jpn.* **1985**, *18*, 105.
(28) Braun, R. L.; Mallon, R. G.; Sohn, H. Y. Analysis of multiple gas-solid reactions during the gasification of char in oil shale blocks. In *Proceedings 14th Oil Shale Symposium*, Colorado School of Mines Press: Golden, CO, 1981; p 289.

DOI: 10.1021/acs.energyfuels.9b01340
Energy Fuels 2019, 33, 7385−7397

(29) Babu, B.; Sheth, P. Modeling and simulation of reduction zone of downdraft biomass gasifier: effect of char reactivity factor. *Energy Convers. Manage.* **2006**, *47*, 2602.
(30) Macak, J.; Malecha, J. Mathematical model for the gasification of coal under pressure. *Ind. Eng. Chem. Process Des. Dev.* **1978**, *17*, 92.
(31) Zahradnik, R. L.; Grace, R. J. Chemistry and physics of entrained coal gasification. *Ind. Eng. Chem. Proc. Des. Dev.* **1974**, *126*, 203.
(32) Kunii, D.; Levenspiel, O. *Fluidization Engineering*, second ed.; Butterworth−Heinemann: Washington Street, USA, 1991.
(33) Bates, R. B.; Altantzis, C.; Ghoniem, A. F. Modeling of biomass char gasification, combustion and attrition kinetics in fluidized beds. *Energy Fuels* **2016**, *30*, 360.
(34) Chang, J.; Yang, S.; Zhang, K. A particle-to-particle heat transfer model for dense gas-solid fluidized bed of binary mixture. *Chem. Eng. Res. Des.* **2011**, *89*, 894.
(35) Gidaspow, D. *Multiphase Flow and Fluidization: Continuum and Kinetics Theory Descriptions*; Academic Press Inc.: San Diego, California, USA, 1994.
(36) Taghipour, F.; Ellis, N.; Wong, C. Experimental and computational study of gas-solid fluidized bed hydrodynamics. *Chem. Eng. Sci.* **2005**, *60*, 6857.
(37) Ranz, W. E. Friction and transfer coefficients for single particles and packed beds. *Chem. Eng. Prog.* **1952**, *48*, 247.
(38) Gunn, D. J. Transfer of heat or mass to particles in fixed and fluidized-beds. *Int. J. Heat Mass Transfer* **1978**, *21*, 467.
(39) Karimipour, S.; Pugsley, T. A critical evaluation of literature correlations for predicting bubble size and velocity in gas-solid fluidized beds - A review. *Powder Technol.* **2011**, *205*, 1.
(40) Agu, C. E.; Tokheim, L.-A.; Eikeland, M.; Moldestad, B. M.E. Improved models for predicting bubble velocity, bubble frequency and bed expansion in a bubbling fluidized bed. *Chem. Eng. Res. Des.* **2019**, *141*, 361.
(41) Agu, C. E.; Pfeifer, C.; Eikeland, M.; Tokheim, L.-A.; Moldestad, B. M.E. Models for predicting average bubble diameter and volumetric bubble flux in deep fluidized beds. *Ind. Eng. Chem. Res.* **2018**, *57*, 2658.
(42) Werther, J. Influence of the bed diameter on the hydrodynamics of gas fluidized beds. *AIChE Symp. Ser.* **1974**, *70*, 53.
(43) Coker, A. K. *Ludwig's Applied Process Design for Chemical and Petroleum Plants*, fourth ed.; 2007; Vol. *1*, p 827−862.
(44) Wilke, C. R. A viscosity equation for gas mixtures. *J. Chem. Phys.* **1950**, *18*, 517.
(45) Li, Y. H.; Chen, Z.; Watkinson, P.; Bi, X.; Grace, J.; Lim, C. J.; Ellis, N. A novel dual-bed for steam gasification of biomass. *Biomass Convers. Biorefin.* **2018**, *8*, 357.
(46) Narvaez, I.; Orio, A.; Aznar, M. P.; Corella, J. Biomass gasification with air in an atmospheric bubbling fluidized bed. Effect of six operational variables on the quality of the produced raw gas. *Ind. Eng. Chem. Res.* **1996**, *35*, 2110.
(47) Jand, N.; Brandani, V.; Foscolo, P. U. Thermodynamic limits and actual product yields and compositions in biomass gasification processes. *Ind. Eng. Chem. Res.* **2006**, *45*, 834.
(48) Gil, J.; Corella, J.; Aznar, M. P.; Caballero, M. A. Biomass gasification in atmospheric and bubbling fluidized bed: Effect of the type of gasifying agent on the product distribution. *Biomass Bioenergy* **1999**, *17*, 389.
(49) Xue, Q.; Fox, R. O. Multi-fluid CFD modeling of biomass gasification in polydisperse fluidized-bed gasifiers. *Powder Technol.* **2014**, *254*, 187.

DOI: 10.1021/acs.energyfuels.9b01340
Energy Fuels 2019, 33, 7385−7397